Optical Engineering

SPIEDigitalLibrary.org/oe

# Corrugated quantum well infrared photodetectors for far infrared detection

Kwong-Kit Choi
Murzy D. Jhabvala
David Forrai
Jason Sun
Darrel Endres

# Corrugated quantum well infrared photodetectors for far infrared detection

**Kwong-Kit Choi**
United States Army Research Laboratory
Adelphi, Maryland 20783
E-mail: kwongkit.choi@us.army.mil

**Murzy D. Jhabvala**
NASA Goddard Space Flight Center
Greenbelt, Maryland 20771

**David Forrai**
L3-Cincinnati Electronics
Mason, Ohio 45040

**Jason Sun**
United States Army Research Laboratory
Adelphi, Maryland 20783

**Darrel Endres**
L3-Cincinnati Electronics
Mason, Ohio 45040

**Abstract.** We have extended our investigation of corrugated quantum well infrared photodetector focal plane arrays (FPAs) into the far infrared regime. Specifically, we are developing the detectors for the thermal infrared sensor (TIRS) used in the Landsat Data Continuity Mission. To maintain a low dark current, we adopted a low doping density of $0.6\times10^{18}$ cm$^{-3}$ and a bound-to-bound state detector. The internal absorption quantum efficiency (QE) is calculated to be 25.4%. With a pixel fill factor of 80% and a substrate transmission of 70.9%, the external QE is 14.4%. To yield the theoretical conversion efficiency (CE), the photoconductive gain was measured and is 0.25 at 5 V, from which CE is predicted to be 3.6%. This value is in agreement with the 3.5% from the FPA measurement. Meanwhile, the dark current is measured to be $2.1\times10^{-6}$ A/cm$^2$ at 43 K. For regular infrared imaging above 8 $\mu$m, the FPA will have an noise equivalent temperature difference (NETD) of 16 mK at 2 ms integration time in the presence of 260 read noise electrons. The highest operability of the tested FPAs is 99.967%. With the CE agreement, we project the FPA performance in the far infrared regime up to 30 $\mu$m cutoff.
 [DOI: 10.1117/1.3578406]

Subject terms: quantum well infrared photodetector; focal plane array; noise equivalent temperature difference.

Paper 110243SSPR received Mar. 10, 2011; revised manuscript received Mar. 25, 2011; accepted for publication Mar. 25, 2011; published online May 12, 2011.

## 1 Introduction

We have developed the corrugated quantum well infrared photodetector focal plane array (C-QWIP FPA) technology for a number of years. Presently, both the theoretical model and the production processes are sufficiently mature such that the FPA properties are well understood in the quantitative manner while high production yield is consistently maintained. In this work, we applied this technology to the NASA Landsat project and obtained satisfactory results. In view of the agreement between theory and experiment in these and other detectors in the long wavelength regime, we extend the C-QWIP model to the far infrared and predict its performance up to 30-$\mu$m cutoff.

## 2 TIRS5 FPA

In this section, we will apply the existing C-QWIP model[1] to one of the FPAs developed for the thermal infrared sensor (TIRS) instrument.[2] To predict the external quantum efficiency $\eta$ of a C-QWIP FPA, the absorption coefficient $\alpha(\lambda)$ of the QWIP material is first calculated for parallel propagating light with a proper polarization. $\alpha(\lambda)$ is given by

$$\alpha(\lambda)=\sum_n \frac{N_D W}{L}\frac{\pi e^2\hbar}{2\sqrt{\varepsilon_h}\varepsilon_0 m^* c} f_n \rho_n(\lambda), \tag{1}$$

where $N_D$ is the doping density in the well, $W$ is well width, $L$ is the quantum well (QW) period length, $f_n$ is the oscillator strength from the ground state to the $n$'th excited state, and $\rho_n$ is the normalized Gaussian broadening for each optical transition. The values of $f_n$ are obtained after solving the eigen energies and eigenfunctions of the structure. The C-QWIP pixel geometry reflects the normally incident light into parallel propagation, with which $\eta$ is given by

$$\eta(V,\lambda)=t_s f_p \eta_{\text{int}}=t_s f_p \kappa \frac{1}{p}\left[t+\frac{e^{-\alpha p}}{2\alpha}(1-e^{2\alpha t})\right]\gamma(V). \tag{2}$$

In Eq. (2), $t_s$ is the substrate transmission, $f_p$ is the pixel fill factor, $\eta_{\text{int}}$ is the internal quantum efficiency, $\kappa$ is a factor proportional to the thickness of the active layer inside a corrugation, $p$ is the pixel linear dimension, $t$ is the corrugation height, and $\gamma(V)$ is the transmission coefficient of a photoelectron traveling out of the quantum well at a bias $V$. The resulting photocurrent $J_p$ generated within a C-QWIP pixel will then be

$$J_p(V,T_B)=\frac{\pi}{4F^2+1} e g(V)\int_{\lambda_1}^{\lambda_2}\eta(V,\lambda)L(T_B,\lambda)d\lambda, \tag{3}$$

where $T_B$ is the scene temperature, $g(V)$ is the photoconductive gain obtained from noise measurement, $\lambda_1$ and $\lambda_2$ are the lower and upper wavelengths encompassing the detector absorption spectrum, $F$ is the $f$-number of the optical system, and $L(T_B,\lambda)$ is the photon spectral radiance.

The QWIP material described below is labeled as TIRS5. It consists of 60 periods of 700 Å $Al_{0.172}Ga_{0.828}As$ and 60 Å GaAs. In order to avoid dopant migration during the material growth, only the center part of the well is doped such that the equivalent $N_D$ is $0.6\times10^{18}$ cm$^{-3}$ in the well. The active QW material is sandwiched between two GaAs contact layers. The top layer is 3.67-$\mu$m thick and the bottom layer is

0091-3286/2011/$25.00 © 2011 SPIE

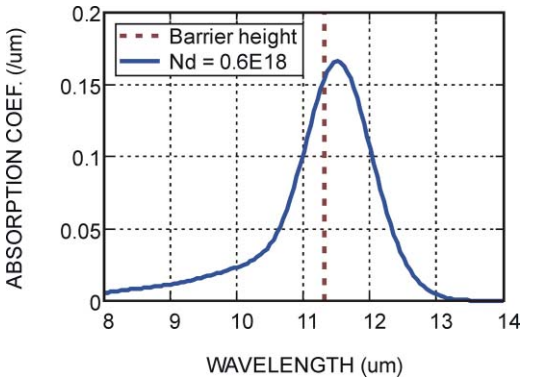


**Fig. 1** The calculated absorption coefficient $\alpha$ of TIRS5. The straight line divides bound-to-bound transitions on the right and bound-to-continuum transitions on the left.

4.15-$\mu$m thick. By applying Eq. (1) to this material, the value of $\alpha$ is shown in Fig. 1. Its peak value is 0.17 $\mu m^{-1}$. The calculation shows that the structure is a bound-to-bound (B-B) state detector because its peak is below the barrier height. The combination of a low doping density and the B-B detector structure ensures a low dark current for this long wavelength detector but with some sacrifice on $\eta$.

Inserting $\alpha(\lambda)$ into Eq. (2), $\eta_{\text{int}}$ and $\eta$ can be obtained. With $p = 25$ $\mu$m, $t = 11$ $\mu$m and $\kappa = 0.69$ for 60 QWs, the peak $\eta_{\text{int}}$ is 25.4%. For uncoated FPAs, $t_s = 0.709$; and assuming $f_p = 0.80$ and $\gamma = 1$ at high bias, the calculated external $\eta$ is shown in Fig. 2, which shows a maximum value of 14.4%. To know the external conversion efficiency (CE) ($\equiv \eta g$), the photoconductive gain $g(V)$ was obtained from the noise measurement and is shown in Fig. 3. At the substrate bias of 5 V, $g$ was measured to be 0.25, with which the peak CE is predicted to be 3.6% as shown in Fig. 2. The material was processed into C-QWIP FPAs and the arrays were hybridized to Indigo 9803 640×512 readout circuits (ROICs). The measured CE from one of the FPAs is shown in Fig. 4. It increases with the applied bias, and at 5 V, the measured CE is 3.5%, which agrees with the prediction of 3.6%. The dashed curve in Fig. 4 is the same curve shown in Fig. 2 but was shifted to a shorter wavelength by 0.35 $\mu$m to match the experimental spectrum. From the agreements on both the magnitude and lineshape, one can assess the accuracy of the detector model in predicting the C-QWIP optical properties. Using the fitted CE spectrum (dashed curve in Fig. 4), the calculated detector photocurrent from Eq. (3) is

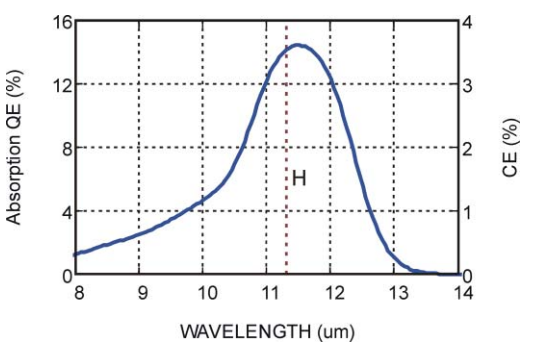


**Fig. 2** The calculated $\eta$ and CE spectra of TIRS5 for $g = 0.25$. $H$ is the barrier height.

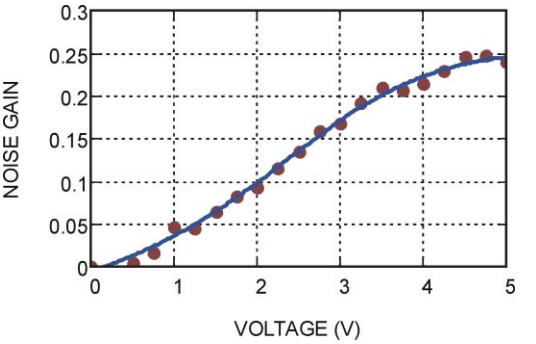


**Fig. 3** The photoconductive gain of TIRS5 obtained from noise measurement.

$1.19\times10^{-4}$ A/cm$^2$ (or $4.62\times10^9$ e$^-$/s/pixel) with F/2 optics and 294 K background when imaging at $\lambda > 8$ $\mu$m.

In addition to the optical properties, the dark current of a C-QWIP can also be modeled and predicted in sufficient accuracy. The dark current transport can be classified into three main mechanisms, which are direct tunneling (DT) between adjacent QWs, thermally assisted tunneling (TAT) near the tip of a tilted barrier under bias and thermionic emission (TE) over the barrier. All of these three transport mechanisms can be incorporated into a single expression,[3] in which

$$
\begin{aligned}
J(V,T) &= \int_{E_1}^{\infty} J(E,V,T)dE, \\
&= \int_{E_1}^{\infty} e\rho f(E,T)\gamma(E,V)v(V)dE, \\
&= \int_{E_1}^{\infty} e\frac{m*}{\pi\hbar^2 L}\frac{\gamma(E,V)}{1+\exp\left(\frac{E-E_F-E_1}{kT}\right)}\frac{\mu V/L}{\sqrt{1+\left(\frac{\mu V}{Lv_{\text{sat}}}\right)^2}}dE.
\end{aligned}
\tag{4}
$$

In Eq. (4), $J(V, T)$ is the measured dark current density, $J(E, V, T)$ is the current density per meV, $\rho$ is the effective three-dimensional density of states in the QW, $f(E, T)$ is the Fermi–Dirac energy distribution, $\gamma$ is the tunneling probability out of the QW, and $v(V)$ is the electron drift velocity. The value of

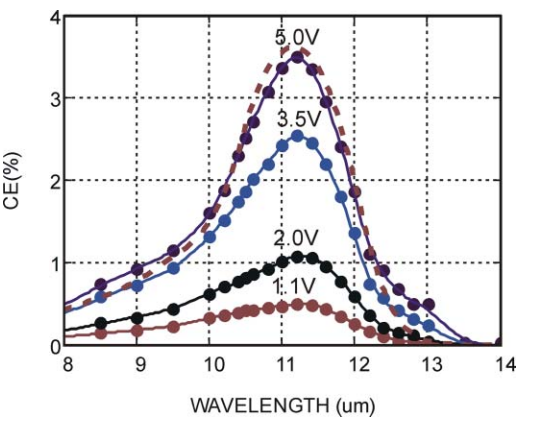


**Fig. 4** Measured spectral conversion efficiency of a TIRS5 FPA at different bias (circles) and the calculated CE (dashed curve) at 5 V, which has been blueshifted by 0.35 $\mu$m.

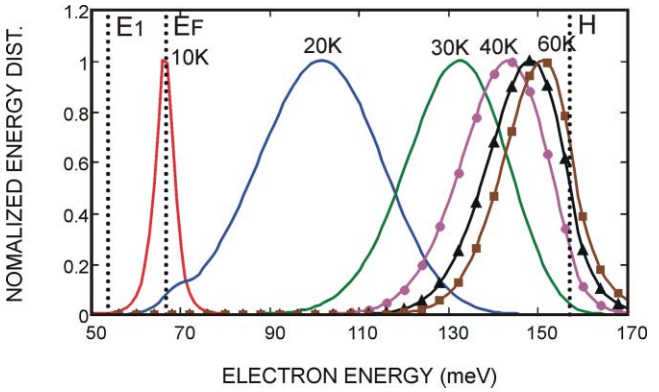


**Fig. 5** The plot shows the energy distribution of the conducting dark electrons at different temperatures. The assumed bias is at 5 V or 83 mV/period. In this plot, $E_1$ is the ground state energy relative to the GaAs band edge, $E_F$ is the Fermi energy, and $H$ is the barrier height of the QW. TAT current dominates in the entire calculated temperature range except at 10 K.

$\gamma$ is given by the usual WKB expression, and $v(V)$ is related to the low field mobility $\mu$ at low bias and the saturation velocity $v_{sat}$ at the high bias as shown in Eq. (4).

At very low $T$, when $f(E, T)$ is essentially 1 for $E < E_F$ and 0 when $E > E_F$, Eq. (4) describes the DT process. When T increases, the finite $f(E, T)$ above $E_F$ created the TAT current. At very high $T$, more electrons can be excited above the barrier with which $\gamma = 1$. TE process then dominates. To visualize their relative contributions at different $T$, $J(E, V, T)$ for the present TIRS5 structure is plotted in Fig. 5 at $V = 83$ mV/period and different T. It is shown that the carrier distribution moves up quickly in energy as T increases and at $T \sim 43$ K, the dark carriers are conducting just below the tip of the tilted barrier.

Figure 6 shows the measured and fitted dark current for TIRS5 C-QWIP test detectors. The three fitted parameters in Eq. (4) are $H = 157.1$ MeV in the WKB expression,

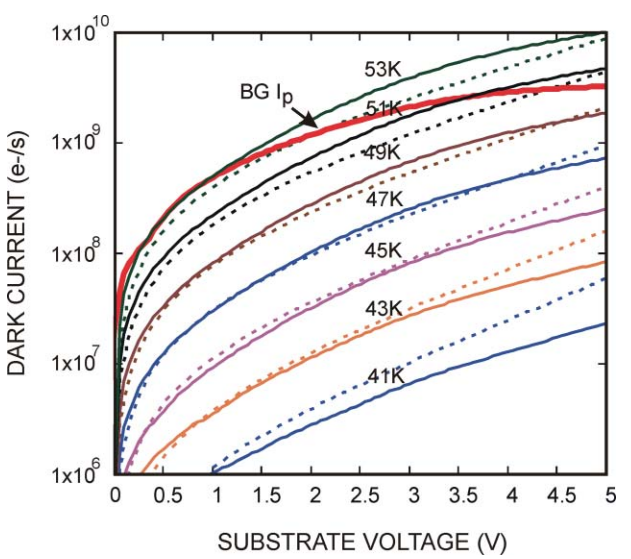


**Fig. 6** The measured dark current (solid curves) of a large area C-QWIP test detector normalized to the pixel area. The dashed curves are the fitted current using Eq. (4). The thick solid curve shows the measured background photocurrent of the test detector.

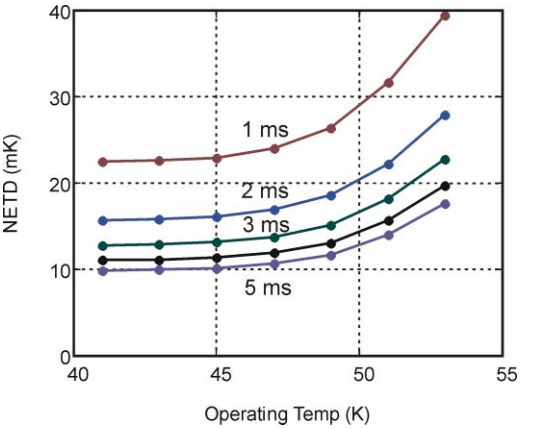


**Fig. 7** The calculated NE$\Delta$T of a TIRS5 FPA operated under different temperatures and integration times for 260 noise electrons, F/2 and 5 V based on the measured photocurrent and dark current.

$\mu = 400$ cm$^2$/Vs, and $v_{sat} = 1\times10^7$ cm/s. The value of $H$ is close to the 163.5 MeV deduced from the spectral response measurement and $v_{sat}$ is the same as the known saturation velocity for GaAs. We found that the present fitted values of $\mu$ and $v_{sat}$ are universally the same for all detectors having $\lambda_c$ ranging from 9 to 13 $\mu$m, showing the consistency of the model. Only for shorter wavelength QWIPs, such as the one at $\lambda_c = 8.6$ $\mu$m, a smaller $\mu$ of 120 cm$^2$/Vs was observed. Figure 6 also shows the background generated photocurrent $J_p$ of the test detector. At 5 V, $J_p$ is observed to be $3.24\times10^9$ e$^-$/s/pixel, which is 70% of the predicted value of $4.62\times10^9$ e$^-$/s/pixel. Since the transmission loss of the KRS-5 window in the optical dewar is 70%, the two measurements thus agree to within experimental error.

With the known $J_p = 4.62\times10^9$ e$^-$/s/pixel, the measured $J_d$ in Fig. 6, and $g = 0.25$ at 5 V, the NE$\Delta$T of a TIRS5 FPA can be estimated from[4]

$$\mathrm{NE}\Delta\mathrm{T} = \frac{1}{C}\left[\left(\frac{2gN_{\mathrm{tot}} + n_{\mathrm{rd}}^2}{N_{\mathrm{tot}}^2}\right)\left(1+\frac{1}{r}\right)^2 + u^2\right]^{1/2}, \qquad (5)$$

where $C = 0.0149$ is the thermal contrast, $N_{\mathrm{tot}}$ is the total number of electrons collected in an integration time $\tau_{\mathrm{int}}$, $n_{\mathrm{rd}} = 260\mathrm{e}^-$ is the measured number of noise electrons, and $r = J_p/J_d$ is the photocurrent to dark current ratio. The parameter $u$ is the spatial nonuniformity, which is assumed to be zero here. Thus, Eq. (5) thus, considers only two noise sources, which are the detector $g$-$r$ noise from both the photocurrent and the dark current and the ROIC noise. The presence of other noise sources such as cooler induced noise and target thermal fluctuations are ignored. Figure 7 shows the expected NE$\Delta$T as a function of operating temperature $T$ for different $\tau_{\mathrm{int}}$. NE$\Delta$T is 16 and 22 mK at $T = 43$ and 51 K, respectively, for $\tau_{\mathrm{int}} = 2$ ms. This result assumes the use of the full spectrum at $\lambda > 8$ $\mu$m. With different adopted filter bandwidths, f/# and detector bias in the TIRS instrument, a different $\tau_{\mathrm{int}}$ may be needed to achieve the same NE$\Delta$T. We also note that the fabricated FPAs typically have very high operability, being in the range of 99.96%.

## 3 LC9 FPA

In this section, we apply the same analysis to a recent 1-megapixel FPA to illustrate the consistency of the model.

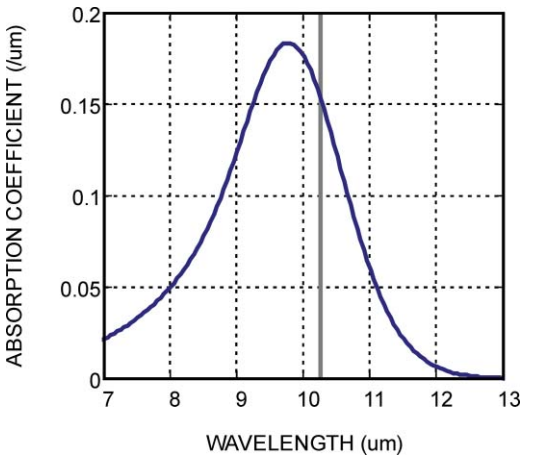


**Fig. 8** The calculated absorption coefficient $\alpha$ of LC9. The straight line divides bound-to-bound transitions on the right and bound-to-continuum transitions on the left.

The FPA is labeled as the LC9 FPA. The material is made of 60 periods of 700 Å $Al_{0.19}Ga_{0.81}As$ and 50Å GaAs. The center part of the well is doped with the equivalent $N_D$ of $1.7\times10^{18}$ $cm^{-3}$ in the well. Since it is a bound to quasibound plus (B-Q+) detector, the spectral width of $\alpha(\lambda)$ in Fig. 8 is wider than that of TIRS5, while the peak value is about the same despite a higher $N_D$. The calculated peak $\eta_{int}$ and $\eta$ are thus about the same as that of TIRS5 and they are 26.1% and 18.8%, respectively. In the $\eta$ estimation, we have assumed $t_s = 0.9$ for an anti-reflection (AR)-coated substrate and $f_p = 0.80$. The value of $\eta$ is shown in Fig. 9. The gain plot is shown in Fig. 10, and at $V = -3$ V, $g = 0.25$. The corresponding calculated CE is then equal to 4.7% at $-3$ V as shown in Fig. 9.

The material was processed into C-QWIP FPAs and the arrays were hybridized to L3-Cincinnati Electronics ROICs, which operate on negative substrate bias, opposite to the Indigo ROICs. The measured CE from one of the FPAs is shown as circles in Fig. 11 up to $-2.5$ V. By fitting this data with the trend of the background photocurrent, CE at $-3$V is deduced to be 4.9%, which agrees with the 4.7% from calculation. The measured FPA CE spectrum is shown as circles in Fig. 9. It agrees quite well with the calculated

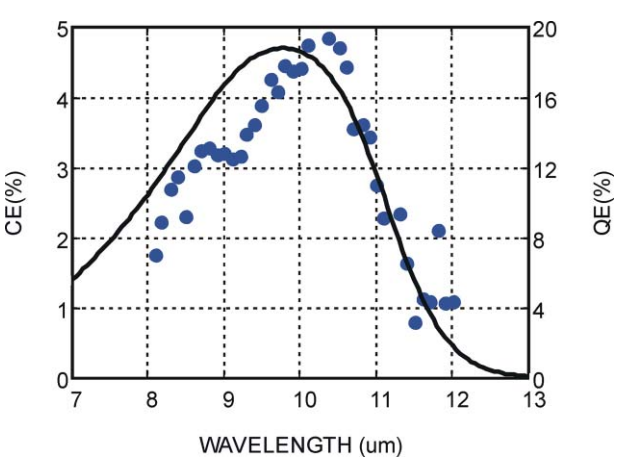


**Fig. 9** Measured spectral conversion efficiency of an LC9 FPA at different bias (circles) and the calculated $\eta$ and CE (solid curve) at $-3$ V.

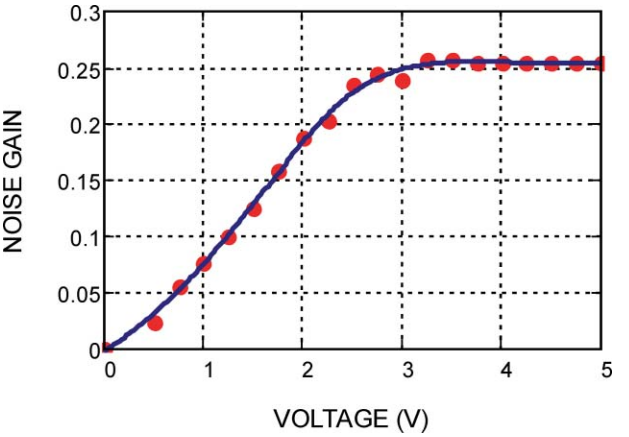


**Fig. 10** The photoconductive gain of LC9 obtained from noise measurement.

spectrum. The sharp decrease of signal in approaching 8 $\mu$m was caused by the presence of an 8-$\mu$m cold filter in the dewar. The average $\eta$ as a function of voltage in Fig. 11 is deduced to be ~20%, in agreement with the expected 18.8% from calculation.

Because of the occurrence of dopant migration during material growth even with localized doping, the *I–V* characteristics of a QWIP show an asymmetry with respect to the bias polarity. Under negative bias, the LC9 material shows a larger dark current $J_d$ than that under positive bias as indicated in Fig. 12. Only the $J_d$ under positive bias fits Eq. (4). The fitting parameters are: $H = 191$ meV from the material design, $\mu = 400$ $cm^2$/Vs and $v_{sat} = 1\times10^7$ cm/s. As a result, the FPA is background limited infrared performance (BLIP) at a lower temperature $T$ of 50 K at $-3$ V rather than 55 K at $+3$ V. In Fig. 12, we also show the FPA pixel dark current at 52 K and photocurrent. They agree with the *I–V* of the large area C-QWIP test detector. Figure 13 shows the calculated NE$\Delta$T based on the observed dark current at $-3$ V. The value of NE$\Delta$T is 12 and 20 mK at $T = 45$ and 52 K, respectively, for $\tau_{int} = 2$ ms. Figure 14 shows an infrared image taken at $T = 52$ K, $-1$ V ,and $\tau_{int} = 2.0$ ms.

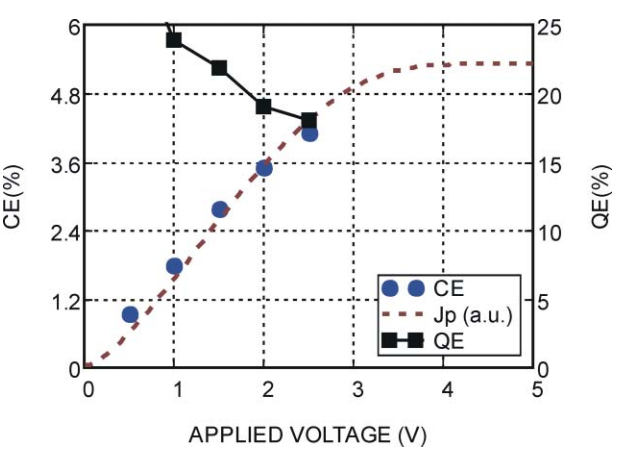


**Fig. 11** The figure shows the measured FPA CE (circles) and the deduced $\eta$ (squares). The dashed curve is the measured background photocurrent and was scaled to fit the CE data. The maximum CE expected to be 5.3% occurred at $-4$ V.

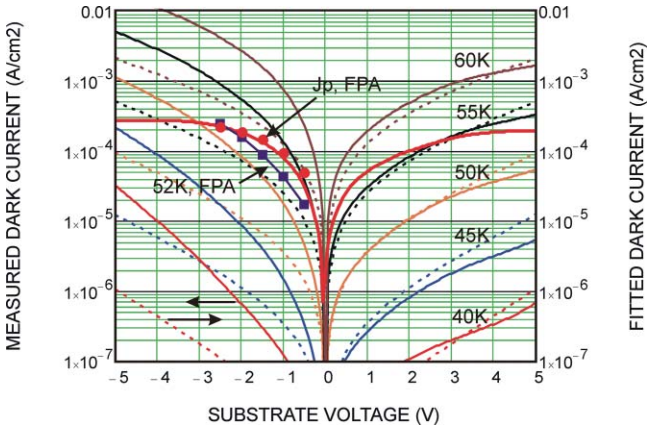


**Fig. 12** Measured dark current (thin solid curves) and photocurrent (thick solid curves) of a C-QWIP test detector. The calculated dark current is shown as dashed curves, which fits the measured data under positive bias. The squares are the measured FPA dark current at 52 K, which fall between the 50 and 55 K test detector data. The circles are the calculated background photocurrent based on the FPA CE spectral measurement.

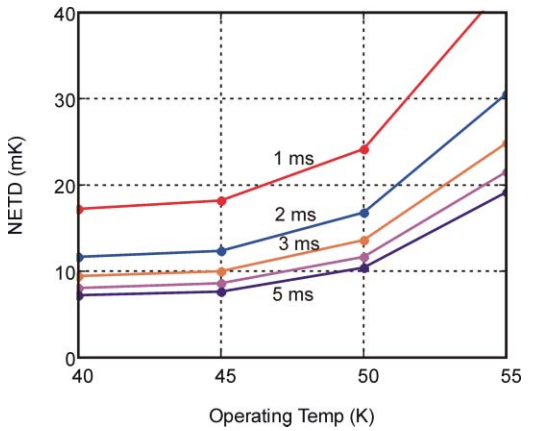


**Fig. 13** The calculated NE$\Delta$T of a LC9 FPA operated under different temperatures and integration times for 900 noise electrons, F/2, and $-3$ V based on the measured photocurrent and dark current.

**Fig. 14** 1-MP infrared image taken by an LC9 FPA at T = 52 K, $-1$ V and $\tau_{int} = 2.0$ ms.

**Fig. 15** 1-MP infrared images taken by (left) an FPA with 9.2-$\mu$m cutoff at 60 K and (right) an FPA with 11.6-$\mu$m cutoff at 40 K, both under the lower $I_d$ polarity.

Although the L3-CE's ROICs operate on the higher $I_d$ polarity in these experimental FPAs, the applied polarity will be reversed on the FPAs produced under L3-CE's unique detector wafer process.[5] In this process, the entire QWIP wafer is first flip-chip bonded to a Si wafer and the substrate of the QWIP wafer is removed. The detector pixels are then created by etching into the detector material using the Si wafer as the substrate. With this upside down material structure, the ROIC biases the detector pixels at the lower $I_d$ polarity. Using this unique process, L3-CE has recently fabricated several FPAs. Figure 15 shows the infrared images taken from two of these 1-MP C-QWIP FPAs operated under the lower $I_d$ polarity.

## 4 Far infrared C-QWIP FPAs

From the above two examples, one can observe that most of the C-QWIP FPA properties can be designed and predicted in high accuracy. In the example below, we venture out to predict the expected FPA performance in the far infrared. The band structure of the material design is shown in Fig. 16. By varying the QW thickness within the superlattice between the two 1000-Å blocking barriers, a wide detection spectrum can be achieved. The $\lambda_c$ of this structure is determined by the bandgap of the two lowest minibands, which can be made small by changing the QW thicknesses. This material design allows a very long $\lambda_c$ (30 $\mu$m in the present example) to be reached without having a very low barrier height to maintain the material uniformity. Figure 17 shows the calculated $\eta_{int}$ for 63 QW periods, which will fill up a corrugation having a base width of 25 $\mu$m. (Each pixel may contain several corrugations in these very long wavelength FPAs.) The peak $\eta_{int}$ is calculated to be 35% for a doping of $0.9\times10^{18}$ cm$^{-3}$. Figure 17 also shows the radiation spectrum of a 110-K blackbody as, for example, encountered on the surface of one of Jupiter's moons, Europa. The proposed detector will be adept in detecting such a cold object.

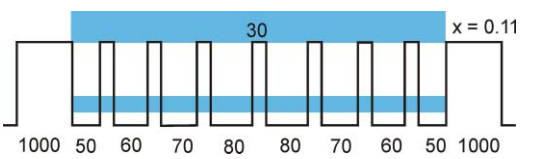


**Fig. 16** The band structure of a quantum well period of a broadband QWIP with $\lambda_c$ equal to 30 $\mu$m. The numerals are the layer thicknesses in angstroms. The aluminum molar ratio is 0.11. The figure also shows the two lowest minibands.

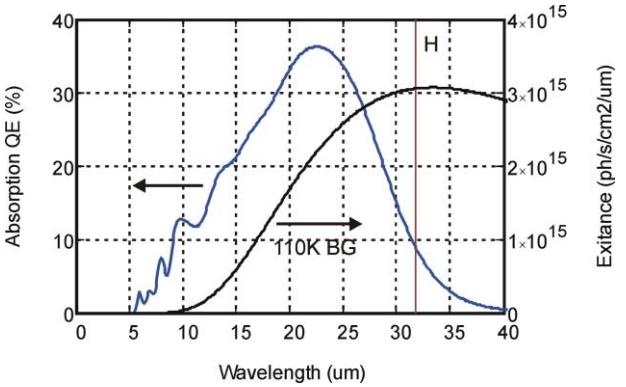


**Fig. 17** The absorption spectrum of the proposed material and the emission spectrum of a 110-K blackbody. The line shows the wavelength corresponding to the photon energy $H - (E_F + E_1) = 101 - 62 = 39$ MeV.

The dark current can be similarly calculated using $\mu = 400$ cm$^2$/Vs, $v_{sat} = 1\times10^7$ cm/s and $H = 101$ MeV, and it is shown in Fig. 18. Figure 18 also shows the background generated photocurrent under $F/2$ for two background temperatures $T_B$. In estimating $J_p$, we have assumed the same gain in Fig. 3 for TIRS5 as they are having a similar number of QWs. In this example, we have assumed a 100% fill factor and substrate transmission for simplicity. Due to the broadband characteristics of this material, the detector photocurrent is about 8 times larger than that of TIRS5 at the same $T_B$ of 300 K. In addition, because of its very long cutoff, $J_p$ is reduced only 100 times when $T_B$ is reduced to 110 K and it still maintains a healthy level of $\sim1\times10^{-5}$ A/cm$^2$. Since the dark current decreases exponentially in $T$, the reduction of $J_p$ translates to less than a 10 K reduction in the BLIP temperature from that with the 300-K background. In the present example, it is BLIP at about 21 K at +3 V. The corresponding NE$\Delta$T of this hypothetical FPA is shown in Fig. 19 assuming 260 noise electrons and a thermal contrast

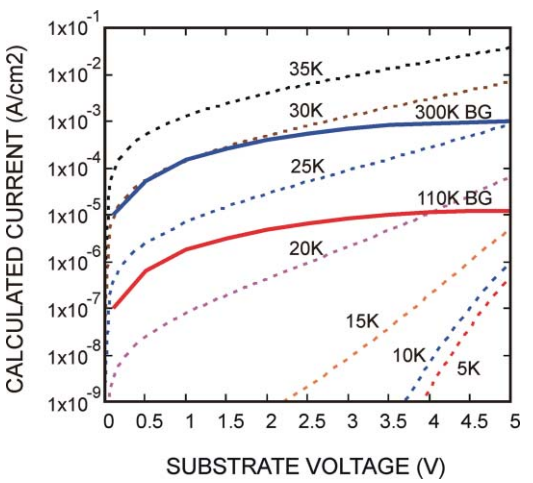


**Fig. 18** The calculated dark current (dashed curves) and the calculated background photocurrent (solid curves) under two background temperatures for a C-QWIP FPA.

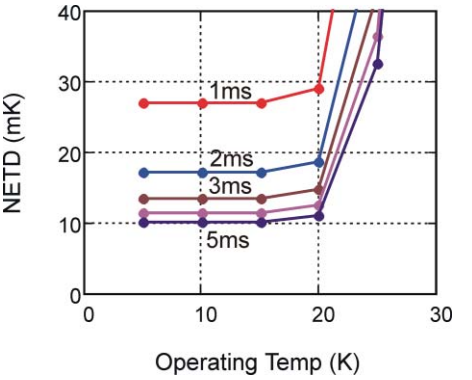


**Fig. 19** The calculated NE$\Delta$T of a hypothetical C-QWIP FPA with $\lambda_c = 30$ $\mu$m operated under different temperatures and integration times for 260 noise electrons, F/2, and 3 V in viewing a 110-K scene.

$C$ of 0.0478 between 5 to 35 $\mu$m at $T_B = 110$ K. Such a camera is expected to resolve a 10 mK temperature difference when operated below 20 K.

## 5 Conclusion

We have applied the present C-QWIP model to two FPAs with cutoffs around 12 $\mu$m and obtained quantitative agreement for both the dark current and photocurrent. Both of these FPAs are competent in high-speed imaging with NE$\Delta$T on the order of 20 mK at 2 ms integration time and T $\sim$ 50 K. The FPA with the higher doping shows a high external quantum efficiency of 20% and a broad spectral width of 3 $\mu$m. By applying the same detector model to the far infrared regime, we found that the C-QWIP FPAs continue to be sensitive in these longer wavelengths albeit requiring a lower operating temperature. The present analysis shows that a C-QWIP camera should be able to provide 10 mK temperature resolution at 5 ms integration time at an operating temperature of 20 K when viewing a 110-K scene. A sensitive and fast camera, together with the promise of reliability, affordability, and uniformity of the GaAs material, will be very useful for space explorations particularly in detecting and observing cold objects. To this end, TIRS on the Landsat mission may only be the first example for QWIP applications in space.

## *References*

1. K. K. Choi, D. P. Forrai, D. W. Endres, and J. Sun, "Corrugated quantum well infrared photodetector focal plane arrays," *IEEE J. Quant. Elect.* **45**, 1255–1264 (2009).
2. M. Jhabvala, D. Reuter, K. Choi, M. Sundaram, C. Jhabvala, A. La, A. Waczynski, and J. Bundas, "The QWIP focal plane assembly for NASA's Landsat Data Continuity Mission," *Proc. SPIE* **76603J 1–13**, (2010).
3. B. F. Levine, C. G. Bethea, G. Hasnain, V. O. Shen, E. Pelve, R. R. Abbott, and S. J. Hsieh, "High sensitivity low dark current 10 $\mu$m GaAs quantum well infrared photodetectors," *Appl. Phys. Lett.* **56**, 851–863 (1990).
4. K. K. Choi, C. J. Chen, A. C. Goldberg, W. H. Chang, and D. C. Tsui, "Performance of corrugated quantum well infrared photodetectors," *Proc. SPIE* **3379**, 441–452 (1998).
5. H. A. Timlin and C. J. Martin, "Method of making electro-optical detector array," US No. 5304500(1994).

Biographies and photographs of the authors not available.